Published in final edited form as:

J Biomech. 2018 January 03; 66: 18–25. doi:10.1016/j.jbiomech.2017.10.031.

Functional MRI Can Detect Changes in Intratissue Strains in a Full Thickness and Critical Sized Ovine Cartilage Defect Model

Deva D. Chan[1,2,§], **Luyao Cai**[1,§], **Kent D. Butz**[3], **Eric A. Nauman**[1,3,4], **Darryl A. Dickerson**[3,4], **Ilse Jonkers**[5], and **Corey P. Neu**[1,6,†]

[1]Weldon School of Biomedical Engineering, Purdue University, West Lafayette, IN 47907

[2]Department of Biomedical Engineering, Rensselaer Polytechnic Institute, Troy, NY 12180

[3]School of Mechanical Engineering, Purdue University, West Lafayette, IN 47907

[4]BioRegeneration Technologies, Inc., West Lafayette, IN 47907

[5]Kinesiology Department, KU Leuven, Leuven, Belgium

[6]Department of Mechanical Engineering, University of Colorado Boulder, Boulder, CO 80309

Abstract

Functional imaging of tissue biomechanics can reveal subtle changes in local softening and stiffening associated with disease or repair, but noninvasive and nondestructive methods to acquire intratissue measures in well-defined animal models are largely lacking. We utilized displacement encoded MRI to measure changes in cartilage deformation following creation of a critical-sized defect in the medial femoral condyle of ovine (sheep) knees, a common *in situ* and large animal model of tissue damage and repair. We prioritized visualization of local, site-specific variation and changes in displacements and strains following defect placement by measuring spatial maps of intratissue deformation. Custom data smoothing algorithms were developed to minimize propagation of noise in the acquired MRI phase data toward calculated displacement or strain, and to improve strain measures in high aspect ratio tissue regions. Strain magnitudes in the femoral, but not tibial, cartilage dramatically increased in load-bearing and contact regions especially near the defect locations, with an average 6.7% ± 6.3%, 13.4% ± 10.0%, and 10.0% ± 4.9% increase in first and second principal strains, and shear strain, respectively. Strain heterogeneity reflected the complexity of the *in situ* mechanical environment within the joint, with multiple tissue contacts defining the deformation behavior. This study demonstrates the utility of displacement encoded

[†]To whom correspondence should be addressed: Corey P. Neu, University of Colorado, Boulder, 1111 Engineering Drive, UCB 427, Boulder, Colorado 80309-0427, Tel: (303) 492-7330, cpneu@colorado.edu.
[§]Denotes equal contribution.

AUTHOR CONTRIBUTIONS

DDC and CPN designed the study. DDC, LC, KDB, IJ, and CPN developed the methodology and collected the data. EAN and DAD contributed key materials. LC, DDC, and CPN performed the analysis. All authors wrote and edited the manuscript.

CONFLICT OF INTEREST

All author certify that they have no affiliations with or involvement in any organization or entity with any financial interest or non-financial interest in the subject matter of materials discussed in this manuscript.

MRI to detect increased deformation patterns and strain following disruption to the cartilage structure in a clinically-relevant, large animal defect model. It also defines imaging biomarkers based on biomechanical measures, in particular shear strain, that are potentially most sensitive to evaluate damage and repair, and that may additionally translate to humans in future studies.

Keywords

elastography; magnetic resonance imaging; cartilage defect; mechanical behavior; dualMRI and quantitative MRI

INTRODUCTION

Noninvasive methods to assay mechanical function, e.g. displacements or strain, are important to elucidate the healthy and diseased states of load-bearing tissues, and to help identify appropriate therapies and tissue-engineered replacements. In articular cartilage, a common load-bearing tissue, altered contact and internal strain distributions often follows traumatic injury (Thambyah and Broom, 2007), progressing ultimately to advanced osteoarthritis (Guilak et al., 2004). The application of modern repair and regeneration technologies, including treatment of full-thickness defects with engineered osteochondral constructs (Panseri et al., 2011), demands that assays be established to define functional (i.e. mechanical) success. Especially important are techniques that allow for the evaluation of tissue biomechanics and function to define the success of candidate repair and regeneration management strategies in animal models and preclinical trials.

Characterization of the mechanical behavior or material properties of load-bearing repair tissues and its tissue environment often requires the excision of samples for *ex vivo* mechanical testing, whereas histological measures of integration of a tissue engineered construct requires sacrifice of the animal for extraction of the construct and surrounding tissues (Calve et al., 2015; Kleemann et al., 2005; Neu et al., 2015). The ability to track the time course of regeneration and tissue function, particularly in well-defined animal models of soft tissue repair (Arzi et al., 2012; Burger et al., 2007; Dyment et al., 2012; Kleemann et al., 2007), would allow for longitudinal assessment of repair and potentially accelerate the development of next-generation technologies. In particular, the ability to measure restoration of strain distributions in damaged tissue regions to accepted normal values could be used as a measure of success of a tissue engineering solution (Neu, 2014), all while promoting the reduction of numbers and refinement of techniques in preclinical animal models.

Functional imaging technologies, such as MRI, can nondestructively assess normal tissue, detect tissue damage, and monitor both tissue degeneration and the progress of repair treatments (Blumenkrantz and Majumdar, 2007; Kim et al., 2016; Neu, 2014). Mechanical function can be visualized using *d*isplacements *u*nder *a*pplied *l*oading with *MRI* (dualMRI), which involves the combined and synchronous actions of exogenous mechanical loading with rapid displacement-encoded MRI to directly measure deformation in soft tissues including healthy human cartilage *in vivo* (Chan et al., 2016; Chan et al., 2009b; Neu and Walton, 2008). Because dualMRI is noninvasive and nondestructive, it is well suited for longitudinal studies of cartilage repair in animal models or human clinical trials. We

therefore hypothesized that dualMRI is sensitive to the subtle changes that may occur in intratissue cartilage strain following the introduction of a critical-sized tissue defect in a clinically-relevant large animal model.

Numerous challenges arise in an effort to establish dualMRI in a large animal model, including difficulties in applying repeatable mechanical loading to the intact joint *in situ*, limitations in spatial resolution required to image thin (i.e. high aspect ratio) tissues like articular cartilage, constraints on total imaging times required to acquire high signal-to-noise ratio (SNR) image data, and limited options available to minimize propagation of noise within complex image (i.e. phase) data prior to calculations of displacements and strain. To overcome these challenges, the objective of this study was to develop a workflow to quantify the mechanical (i.e. displacement and strain) changes that result from the introduction of a cartilage defect in an ovine model system. Using dualMRI, and newly developed image post-processing methods, we visualized the displacement and strain patterns throughout the femoral cartilage and meniscal and tibial counterfaces, before and following introduction of the defect, to detect whether deformation patterns consistently deviated from those observed in the intact joint.

METHODS

Four ovine stifle (left) joints (of average market weight: 45.4 kg) were obtained from a local abattoir and frozen immediately after slaughter. Prior to the experiment, each joint was slowly thawed at 4°C, and excess tissue was trimmed from the stifle without compromising the joint capsule. The joints were flexed at 50° to replicate the stance phase of quadruped gait (Tapper et al., 2004). The tibia and femur were potted at this flexion angle with polymethylmethacrylate to allow for attachment to a custom MRI-compatible loading device, similar to previously published designs (Chan and Neu, 2012; Chan et al., 2009a), which was secured at the isocenter of a 9.4T Biospec MRI scanner (Bruker Medical GmbH, Ettlington, Germany) for imaging experiments (Figure 1). Joints were wrapped in gauze wetted with phosphate-buffered saline (PBS) and then in plastic wrap to prevent desiccation during imaging.

Prior to mechanical loading, standard morphometric MR images were acquired using a three-dimensional (2D multislice) fast spin echo (RARE) protocol in a sagittal view. Imaging parameters included effective echo time/repetition time (TE/TR) = 30.56/6000 ms, field of view (FOV) = 64.0×64.0 mm^2, spatial resolution = 250×250 μm, slice thickness = 1.5 mm, and number of slices = 9. From these images, we were able to select a slice in the sagittal view that visualized the most distal aspect of the medial condyle, which was used for all subsequent analyses (Figure 1B). Additionally, morphometric images allowed us to estimate the average thicknesses for femur and tibial cartilage tissues using manual measurements with common image processing software packages (ImageJ), in addition to maximum widths of the distal femur (in a coronal view) to enable comparison of individual sheep.

Each joint was cyclically loaded to 445 N (i.e., one-times typical body weight) for 2.0 seconds within a 5.0 second total cycle duration, with loads transferred through the tibia to

the femur. Cine acquisitions using true fast imaging with steady state precession (TrueFISP) were performed to visualize the joint in undeformed and deformed configurations with flip angle = 25°, TE/TR = 1.65/3.30 ms, and aforementioned FOV and spatial resolution. Cine images were acquired approximately every 50 loading cycles, and subtraction of consecutive images of the deformed configuration was used to determine whether the load-displacement response had approached the quasi-steady state needed to minimize motion artifacts (Chan and Neu, 2012; Martin et al., 2009). Once the quasi-steady state displacement response was achieved (Neu and Hull, 2003; Zhang et al., 2015), after approximately 400 loading cycles in this *in situ* experimental configuration, imaging was synchronized with cyclic compressions for dualMRI (Chan and Neu, 2012).

dualMRI was performed using careful timing of exogenous cyclic compression to displacement encoding with stimulated echoes (DENSE (Aletras et al., 1999)) and a TrueFISP acquisition (Chan and Neu, 2012; Neu and Walton, 2008) (Figure 1C). Within each loading cycle, the tissue was encoded with magnetic field gradients prior to loading and then un-encoded after a time delay (i.e. mixing time) during a period of constant mechanical loading, leaving a phase-difference signal that was directly proportional to the overall change in position. Artifacts were reduced using both cosine and sine modulation (CANSEL) of radiofrequency pulses (Epstein and Gilson, 2004) and three complementary TrueFISP acquisitions with different phase advance angles (Chan and Neu, 2012). Tibial and femoral regions of interest (ROIs) and image masks were identified within the image to permit displacement calculations as previously described (Chan and Neu, 2012; Neu and Walton, 2008).

dualMRI was implemented, first in intact joints (Figure 1D), using an encoding gradient moment of 0.65π rad/mm and a mixing time of 600 ms (Chan and Neu, 2012), for a total imaging time of 24 minutes after quasi-steady state was achieved. Encoding gradients were applied in the loading (y) and transverse (x) directions to provide in-plane displacements in the sagittal imaging plane.

After imaging the intact joint, specimens were removed to create 8-mm diameter, 5-mm deep, critical-sized defect (Schlichting et al., 2008) at the most distal aspect of the medial condyle (Figure 1E). Each joint was opened using a single medial parapatellar incision in the superior-inferior direction, with careful attention to not alter or damage primary stabilizing structures (e.g. ligaments, menisci) in the stifle joint. The most distal aspect of the medial condyle was identified via inspection and marked for creation of the defect using a flat-bottomed drill bit. Each joint was flushed with PBS both before and after suturing, and a PBS and protease inhibitor cocktail solution was introduced into the joint capsule. The joint was then repositioned in the loading apparatus for another set of imaging experiments as outlined above. Importantly, placement of the defect in the most distal aspect of the condyle lead to its location adjacent to tibial cartilage in two of the four joints, and adjacent to the meniscus in the other two joints. The variation in defect placement within the joint contributed to inter-specimen variation observed (discussed subsequently).

dualMRI was implemented a second time in joints with a critical-sized defect present (Figure 1E), using imaging parameters identical to those described previously. Registration

of MR images from the (intact or defect) joints was accomplished in part due to the use of the same loading device and placement protocol. Additionally, we ensured that the same image slice was selected for dualMRI, using a careful check of cartilage and joint morphology from morphometric images.

Displacements and strains within the femoral and tibial articular cartilage ROIs were computed, as described previously (Chan and Neu, 2012; Neu and Walton, 2008). Raw displacement fields within each ROI were smoothed using a locally-weighted linear regression method (LOWESS) in MATLAB (The Mathworks, Natick, MA) and, for comparison, by Gaussian smoothing (Chan et al., 2012). For smoothing by LOWESS, least absolute residuals (LAR) were utilized to make the process resistant to outliers due to the noise. The window size for calculating local weight was set to be 200 pixels for consistency among different regions of interest, occupying around 40% pixels for the tibia ROI and 20% pixels for the femur ROI.

Green-Lagrange strains – in the loading direction (E_{yy}), transverse to loading (E_{xx}), and in shear (E_{xy}) – were computed from the discrete displacement fields (Geers et al., 1996), also permitting the calculation of principal strains (E_{p1}, E_{p2}), and max shear strain (E_{sm}). Intact and defect joints were compared by examining the maximum principal strains in the tibial and femoral ROIs which cover the whole cartilage tissue. Maximum strains were also computed in the preserved cartilage-cartilage contact regions (i.e. regions not removed by the surgery and marked red in Figure 2A) within the femoral and tibial ROIs, which were segmented manually. Relative changes in average strains within the tissue ROIs were computed, and data was presented as mean ± standard deviation. Paired t-tests were used to evaluate changes in strain values following defect placement, with a significance level of $p<0.05$. The Anderson-Darling test was used to confirm data normality considering a relatively small sample size was utilized.

RESULTS

dualMRI was accomplished in intact joints and after creation of full-thickness defects (Figure 2). The cartilage-cartilage contact regions that were preserved after creation of the defect varied for each specimen, allowing for visualization of deformation patterns with respect to locations of tissue damage (Figure 2A). The maximum widths of the distal part of the femur in the sagittal plane were measured to be 244, 216, 228, 183 mm for specimens one through four, respectively. At contact regions, the average thickness of femoral cartilage and tibia cartilage were measured to be 0.98 mm ± 0.05 mm and 1.30 mm ± 0.18 mm respectively. In-plane displacements were dominated by rigid body motion resulting from compressive loading and motion of tibia and contact with the femur (Figure 2B). As opposed to Gaussian smoothing, which alters the gradient at edges for thin masks, LOWESS smoothing did not show a systematic bias, allowing for visualization of through-thickness displacement patterns reflecting cartilage-cartilage contact (Figure 2C).

Green-Lagrange strains, computed from smoothed displacements (Figure 3A), and principal strains were heterogeneous throughout the cartilage (Figure 3B). Maximum magnitudes of principal strains and max shear strains in both full ROIs and contact regions of the sheep

specimens generally showed an increase in magnitude with the creation of a defect (Figure 4A). In particular, zones of high strain were localized in the transition between cartilage-cartilage and cartilage-meniscus contact, especially in the femoral cartilage. Averaged across specimens, maximum first principal strains increased from 6.1% to 12.8% in contact region of femoral cartilage with defect (p=0.121), but remained relatively unchanged (7.8% to 7.6%, respectively; p=0.973) in tibial contact regions (Tables 1 and 2). Second principal strains also reflected a shift towards increased magnitude, changing from −6.8% to −20.2% in contact region of femoral cartilage (p=0.078), but only −6.5% to −7.6% in tibial ROIs (p=0.615). Maximum shear strains significantly increased with defect in the femoral (6.5% to 16.5%; p=0.026) but not tibial contact region (7.1% to 7.6%; p=0.830), again also with localized maximum values in the cartilage-to-meniscus contact transition (Figure 4A).

DISCUSSION

The purpose of this study was to test whether dualMRI is sensitive to the subtle changes that may occur in intratissue cartilage strain following the introduction of a critical-sized tissue defect in a clinically-relevant large animal model. Compared to cartilage explants (Neu and Walton, 2008) and intact juvenile joints (Chan et al., 2009b), the use of intact adult joints for dualMRI presents a number of technical challenges. Imaging of intact animal joints requires a large field of view and a corresponding decreased spatial resolution in order to achieve reasonable imaging times. However, the images must still provide adequate spatial resolution through the thickness of relatively thin (i.e. high aspect ratio) cartilage. Additionally, internal deformations are expected to be lower in adult joints, due to decreased cartilage thickness and increased stiffness in weight-bearing areas with maturation (Brommer et al., 2005). The stress of the cartilage was estimated to be 553 kPa from the 445 N load and average estimated contact area of 804 mm^2, which is far below the 35 MPa stress known to damage chondrocytes (Clements et al., 2001; Seedhom, 2006). Also, since the joints were harvested and imaged in the same day, proteoglycan loss was expected to be minimal or negligible (Patwari et al., 2007). Moreover, the study of abnormal joints by dualMRI or elastography is completely unexplored, motivating the need to determine intratissue strains prior to *in vivo* studies of defects and repair in animals or humans.

Improving upon the previously utilized Gaussian smoothing (Chan et al., 2012), LOWESS smoothing of raw displacement data for the estimation of strains largely preserved the through-thickness displacement gradient within the thin cartilage (Figure 2C), minimizing edge bias. Areas of high strain were observed in the transition areas between the cartilage-cartilage and cartilage-meniscus contact areas, even in the intact joint (Figure 3). This could be due to the change in contact deformation reflecting stiffer cartilage-meniscus and cartilage-cartilage behavior. The creation of an osteochondral defect was expected to introduce a more intense change in contact deformation behavior in the tibial cartilage opposite of the femoral defect, which would no longer be in contact with any tissue (Gratz et al., 2008). Individually, most maximum principal strain magnitudes increased with the creation of the defect, as expected (Figure 4A), more than doubling on average in the femoral cartilage. Overall, displacements and strains qualitatively changed with the creation of the defect, as supported by previous studies (Braman et al., 2005; Gratz et al., 2009). However, the lack of observed changes in tibial cartilage may be due to effective distribution

of mechanical force through the meniscus and other structures of the intact knee. A concomitant loss of meniscus structure with cartilage defect may be expected to further alter mechanical load transmission and strain patterns throughout the tibial cartilage. It is important to note that with similar defect sizes, the small size (maximum width) of the femur measured from sheep 4 may contribute to the large maximum shear strain changes in femur (Table 2).

The location and placement of the osteochondral defect may affect the variability of strains observed in this study, with contributions to strain variability likely due to the meniscus and geometry variation. While consistent trends in maximum principal and shear strains in the contact regions of femoral cartilage were observed (Figure 4, Tables 1 and 2), variations between specimens persisted. For example, in one specimen (Sheep 1), the defect was created in the middle of the cartilage-cartilage contact region, leaving minimal cartilage-cartilage contact within the imaged plane. Similarly, minimum principal strain and maximum shear strain in the femoral ROI of this sheep followed different magnitudes compared to other specimen, which could be associated with the lack of direct contact with the tibial cartilage. For the specimens with preserved cartilage-cartilage contact, the principal strain magnitudes followed more consistent trends, reflecting the likely increase in stress resulting from a reduction in contact area (Figure 4A). Additionally, in another specimen (Sheep 4, defect) the maximum and minimum principal strains were both in compression (negative). This result, in a defected joint, could reflect the anisotropic or incompressible nature of cartilage, with significant expansion out of plane. This data suggests that, in addition to the necessity of uniform placement of cartilage defects across animals in preclinical trails to achieve consistent results, the choice of location of the defects with respect to other joint structures, and perhaps also the three-dimensional nature of the contact, must be carefully considered in preclinical trials of cartilage repair efforts.

Although dualMRI permitted the observation of differences in the strain fields after defect creation, it is important to note some limitations of this *ex vivo* animal model. Because of variations in joint sizes and geometry, the location of the preserved cartilage-cartilage contact region within the joint was not consistent between specimens, despite the use of a consistent protocol and anatomical markers to place the defect. Also, although using the same joint allows for repeatable positioning, protease inhibition was then necessary to prevent biochemical degradation and preserve cartilage integrity through the duration of experiments. We did not perform multiple imaging sessions on the same joints, without defect placement, which would in future studies provide an additional control for the results observed herein. Additionally, the *ex vivo* joint was imaged immediately after defect creation, so no time effects or healing response can be observed. However, these results still likely represent the mechanical conditions that exist immediately after surgery or acute injury. Finally, because of the large field of view required to encompass the full joint, the lower spatial resolution of this study is a further limitation, especially when compared to studies that image only a cartilage explant (Braman et al., 2005; Gratz et al., 2008, 2009; Wong and Sah, 2010). The resolution used in this study, however, is similar to what is achievable on the clinical MRI systems that would be used for longitudinal *in vivo* studies (Chan et al., 2016). In addition, alternative devices may improve the *in situ* loading

repeatability following defect placement or damage, and better correlate with histological analyses (Nebelung et al., 2017).

Despite the limitations of this study, dualMRI holds key advantages over other techniques that have been used to examine the mechanical behavior of cartilage near a defect (Braman et al., 2005; Gratz et al., 2008, 2009; Wong and Sah, 2010). As a noninvasive imaging modality, MRI provides the ability to visualize the internal deformations and strains of cartilage explants with and without tissue engineered implants (Neu et al., 2009; Neu and Walton, 2008). Because dualMRI can be used within intact joints (Chan et al., 2011; Chan et al., 2009a, b), there is potential to study clinical repair *in vivo* in longitudinal animal and human studies that are not possible if tissue has to be excised for testing following traditional methods. Moreover, it may be possible to define critical changes in specific strain measures, or strain measures that exceed certain thresholds, as imaging biomarkers that reflect underlying disease pathology. We have noted, in particular, shear strain as a potentially potent biomarker, based on changes observed in this study following defect, and in light of the large dynamic range observed during compressive loading to the human knee *in vivo*, compared to other strain measures (Chan et al., 2016). Our results therefore allow us to determine whether thresholds for healthy performance of cartilage, defined by strain, may uniquely understand or predict the health of the tissue. Finally, our study allows for comparisons of strain measures to multicontrast MRI measures (e.g. relaxivity data like T2 or T1rho) (Griebel et al., 2014). For example, cyclic loading utilized in our study likely leads over time to compaction of deforming cartilage, which would be expected to change relaxivity values (e.g. lower T2). In this sense, common relaxivity techniques could possibly also serve as surrogates for strain.

Future work currently aims toward utilizing *in vivo* imaging capabilities (Chan et al., 2016) in studies to evaluate and monitor the mechanical changes that occur with tissue damage and repair. Longitudinal animal studies would likely significantly reduce the number of animals needed to test a particular treatment paradigm. The use of dualMRI for clinical trials has the potential not only to reduce the number of subjects necessary for a study but also to assess repair tissue integrity and function along various time points after treatment. This study represents progress towards that goal by demonstrating that changes to mechanical behavior (i.e. increases in strain) with the creation of a full-thickness cartilage defect can be visualized and quantified noninvasively and nondestructively with dualMRI.

In summary, noninvasive dualMRI in sheep stifles showed that principal strain and maximum shear strain magnitudes generally increased with the creation of a full-thickness cartilage defect, particularly in the femoral cartilage. Although limited by the lack of a repair response characteristic of sheep studies *in vivo*, this *ex vivo* study demonstrates the feasibility of noninvasive MRI for the measurement of mechanical behavior in articular cartilage to monitor changes in translational, large animal models of cartilage damage and repair.

Acknowledgments

Research Sponsors: BioRegeneration Technologies, Inc.; NIH S10 RR019920-01; NIH R01 AR063712, R21 AR066230, OVPR Research Incentive Grant.

This research was funded in part by Alfred Mann Institute, NSF CMMI 1100554 (CPN and EAN), NIH R01 AR063712, R21 AR064178, and OVPR Research Incentive Grant (CPN). The study was performed at the Center for Basic Magnetic Resonance Research, North Shore University HealthSystem, Evanston, IL, on equipment funded in part by NIH S10 RR019920-01.

References

Aletras AH, Ding S, Balaban RS, Wen H. DENSE: displacement encoding with stimulated echoes in cardiac functional MRI. J Magn Reson. 1999; 137:247–252. [PubMed: 10053155]

Arzi B, Wisner ER, Huey DJ, Kass PH, Hu J, Athanasiou KA. A proposed model of naturally occurring osteoarthritis in the domestic rabbit. Lab Anim (NY). 2012; 41:20–25.

Blumenkrantz G, Majumdar S. Quantitative magnetic resonance imaging of articular cartilage in osteoarthritis. Eur Cell Mater. 2007; 13:76–86. [PubMed: 17506024]

Braman JP, Bruckner JD, Clark JM, Norman AG, Chansky HA. Articular cartilage adjacent to experimental defects is subject to atypical strains. Clin Orthop Relat Res. 2005:202–207.

Brommer H, Brama PA, Laasanen MS, Helminen HJ, van Weeren PR, Jurvelin JS. Functional adaptation of articular cartilage from birth to maturity under the influence of loading: a biomechanical analysis. Equine Vet J. 2005; 37:148–154. [PubMed: 15779628]

Burger C, Mueller M, Wlodarczyk P, Goost H, Tolba RH, Rangger C, Kabir K, Weber O. The sheep as a knee osteoarthritis model: early cartilage changes after meniscus injury and repair. Lab Anim. 2007; 41:420–431. [PubMed: 17988437]

Calve S, Ready A, Huppenbauer C, Main R, Neu CP. Optical clearing in dense connective tissues to visualize cellular connectivity in situ. PLoS One. 2015; 10:e0116662. [PubMed: 25581165]

Chan DD, Cai L, Butz KD, Trippel SB, Nauman EA, Neu CP. In vivo articular cartilage deformation: noninvasive quantification of intratissue strain during joint contact in the human knee. Sci Rep. 2016; 6:19220. [PubMed: 26752228]

Chan DD, Khan SN, Ye XJ, Curtiss SB, Gupta MC, Klineberg EO, Neu CP. Mechanical Deformation and Glycosaminoglycan Content Changes in a Rabbit Annular Puncture Disc Degeneration Model. Spine. 2011; 36:1438–1445. [PubMed: 21270702]

Chan DD, Neu CP. Transient and Microscale Deformations and Strains Measured under Exogenous Loading by Noninvasive Magnetic Resonance. PLoS One. 2012; 7:e33463. [PubMed: 22448245]

Chan DD, Neu CP, Hull ML. Articular cartilage deformation determined in an intact tibiofemoral joint by displacement-encoded imaging. Magn Reson Med. 2009a; 61:989–993. [PubMed: 19189290]

Chan DD, Neu CP, Hull ML. In situ deformation of cartilage in cyclically loaded tibiofemoral joints by displacement-encoded MRI. Osteoarthritis Cartilage. 2009b; 17:1461–1468. [PubMed: 19447213]

Chan DD, Toribio D, Neu CP. Displacement smoothing for the precise MRI-based measurement of strain in soft biological tissues. Comput Methods Biomech Biomed Engin. 2012

Clements KM, Bee ZC, Crossingham GV, Adams MA, Sharif M. How severe must repetitive loading be to kill chondrocytes in articular cartilage? Osteoarthritis Cartilage. 2001; 9:499–507. [PubMed: 11467899]

Dyment NA, Kazemi N, Aschbacher-Smith LE, Barthelery NJ, Kenter K, Gooch C, Shearn JT, Wylie C, Butler DL. The relationships among spatiotemporal collagen gene expression, histology, and biomechanics following full-length injury in the murine patellar tendon. J Orthop Res. 2012; 30:28–36. [PubMed: 21698662]

Epstein FH, Gilson WD. Displacement-encoded cardiac MRI using cosine and sine modulation to eliminate (CANSEL) artifact-generating echoes. Magn Reson Med. 2004; 52:774–781. [PubMed: 15389939]

Geers MGD, de Borst R, Brekelmans WAM. Computing strain fields from discrete displacement fields in 2D-solids. Int J Solids Struct. 1996; 33:4293–4307.

Gratz KR, Wong BL, Bae WC, Sah RL. The effects of focal articular defects on intra-tissue strains in the surrounding and opposing cartilage. Biorheology. 2008; 45:193–207. [PubMed: 18836224]

Gratz KR, Wong BL, Bae WC, Sah RL. The effects of focal articular defects on cartilage contact mechanics. J Orthop Res. 2009; 27:584–592. [PubMed: 18979528]

Griebel AJ, Trippel SB, Emery NC, Neu CP. Noninvasive assessment of osteoarthritis severity in human explants by multicontrast MRI. Magn Reson Med. 2014; 71:807–814. [PubMed: 23553981]

Guilak F, Fermor B, Keefe FJ, Kraus VB, Olson SA, Pisetsky DS, Setton LA, Weinberg JB. The role of biomechanics and inflammation in cartilage injury and repair. Clin Orthop Relat Res. 2004:17–26.

Kim W, Ferguson VL, Borden M, Neu CP. Application of Elastography for the Noninvasive Assessment of Biomechanics in Engineered Biomaterials and Tissues. Ann Biomed Eng. 2016; 44:705–724. [PubMed: 26790865]

Kleemann RU, Krocker D, Cedraro A, Tuischer J, Duda GN. Altered cartilage mechanics and histology in knee osteoarthritis: relation to clinical assessment (ICRS Grade). Osteoarthritis Cartilage. 2005; 13:958–963. [PubMed: 16139530]

Kleemann RU, Schell H, Thompson M, Epari DR, Duda GN, Weiler A. Mechanical behavior of articular cartilage after osteochondral autograft transfer in an ovine model. Am J Sports Med. 2007; 35:555–563. [PubMed: 17293465]

Martin KJ, Neu CP, Hull ML. Quasi-steady-state displacement response of whole human cadaveric knees in a MRI scanner. J Biomech Eng. 2009; 131:081004. [PubMed: 19604016]

Nebelung S, Post M, Raith S, Fischer H, Knobe M, Braun B, Prescher A, Tingart M, Thuring J, Bruners P, Jahr H, Kuhl C, Truhn D. Functional in situ assessment of human articular cartilage using MRI: a whole-knee joint loading device. Biomech Model Mechanobiol. 2017

Neu CP. Functional imaging in OA: role of imaging in the evaluation of tissue biomechanics. Osteoarthritis Cartilage. 2014; 22:1349–1359. [PubMed: 25278049]

Neu CP, Arastu HF, Curtiss S, Reddi AH. Characterization of engineered tissue construct mechanical function by magnetic resonance imaging. J Tissue Eng Regen Med. 2009; 3:477–485. [PubMed: 19530259]

Neu CP, Hull ML. Toward an MRI-based method to measure non-uniform cartilage deformation: an MRI-cyclic loading apparatus system and steady-state cyclic displacement of articular cartilage under compressive loading. J Biomech Eng. 2003; 125:180–188. [PubMed: 12751279]

Neu CP, Novak T, Gilliland KF, Marshall P, Calve S. Optical clearing in collagen-and proteoglycan-rich osteochondral tissues. Osteoarthritis Cartilage. 2015; 23:405–413. [PubMed: 25454370]

Neu CP, Walton JH. Displacement encoding for the measurement of cartilage deformation. Magn Reson Med. 2008; 59:149–155. [PubMed: 18050342]

Panseri S, Russo A, Cunha C, Bondi A, Di Martino A, Patella S, Kon E. Osteochondral tissue engineering approaches for articular cartilage and subchondral bone regeneration. Knee Surg Sports Traumatol Arthrosc. 2011

Patwari P, Cheng DM, Cole AA, Kuettner KE, Grodzinsky AJ. Analysis of the relationship between peak stress and proteoglycan loss following injurious compression of human post-mortem knee and ankle cartilage. Biomech Model Mechanobiol. 2007; 6:83–89. [PubMed: 16715319]

Schlichting K, Schell H, Kleemann RU, Schill A, Weiler A, Duda GN, Epari DR. Influence of scaffold stiffness on subchondral bone and subsequent cartilage regeneration in an ovine model of osteochondral defect healing. Am J Sports Med. 2008; 36:2379–2391. [PubMed: 18952905]

Seedhom BB. Conditioning of cartilage during normal activities is an important factor in the development of osteoarthritis. Rheumatology (Oxford). 2006; 45:146–149. [PubMed: 16287918]

Tapper JE, Ronsky JL, Powers MJ, Sutherland C, Majima T, Frank CB, Shrive NG. In vivo measurement of the dynamic 3-D kinematics of the ovine stifle joint. J Biomech Eng. 2004; 126:301–305. [PubMed: 15179862]

Thambyah A, Broom N. On how degeneration influences load-bearing in the cartilage-bone system: a microstructural and micromechanical study. Osteoarthritis Cartilage. 2007; 15:1410–1423. [PubMed: 17689989]

Wong BL, Sah RL. Effect of a focal articular defect on cartilage deformation during patello-femoral articulation. J Orthop Res. 2010; 28:1554–1561. [PubMed: 20602462]

Zhang L, Miramini S, Smith DW, Gardiner BS, Grodzinsky AJ. Time evolution of deformation in a human cartilage under cyclic loading. Ann Biomed Eng. 2015; 43:1166–1177. [PubMed: 25331101]

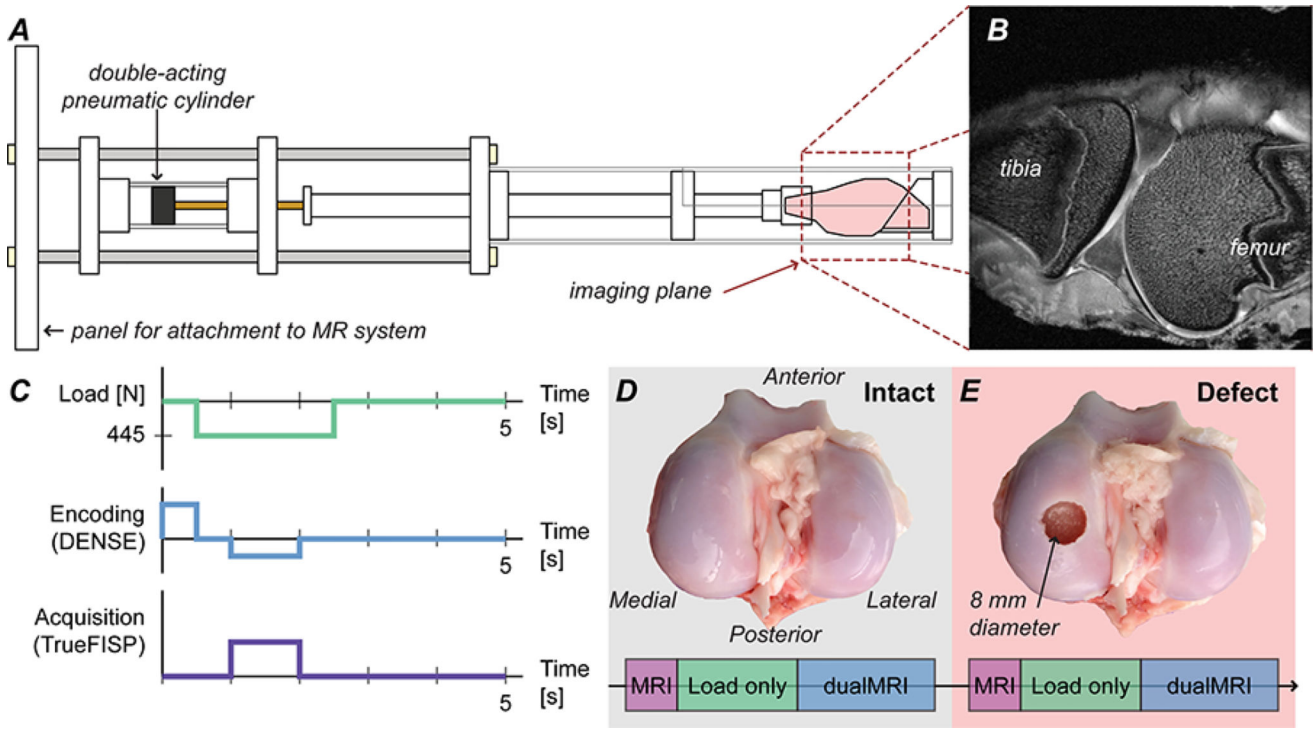

Figure 1. Experimental setup for intact and defect joints

The sheep stifles were placed in an MRI-compatible cyclic loading device to compress joint specimen during the MRI acquisition [*A*]. The sagittal imaging plane was chosen to overlap with the most distal point of the medial femoral condyle in the load-bearing region of the joint; a representative specimen is shown [*B*]. After standard MRI scans, preconditioning with cyclic loading and dualMRI (cyclic loading synchronized with displacement encoded MRI) experiments [*C*] were performed on an intact joint [*D*]. An 8-mm diameter full-thickness (5 mm) osteochondral defect was created at the most distal aspect of the medial condyle [*E*] prior to imaging the defect condition. Joints are shown open for illustrative purposes only, and remained closed with all ligaments intact during testing.

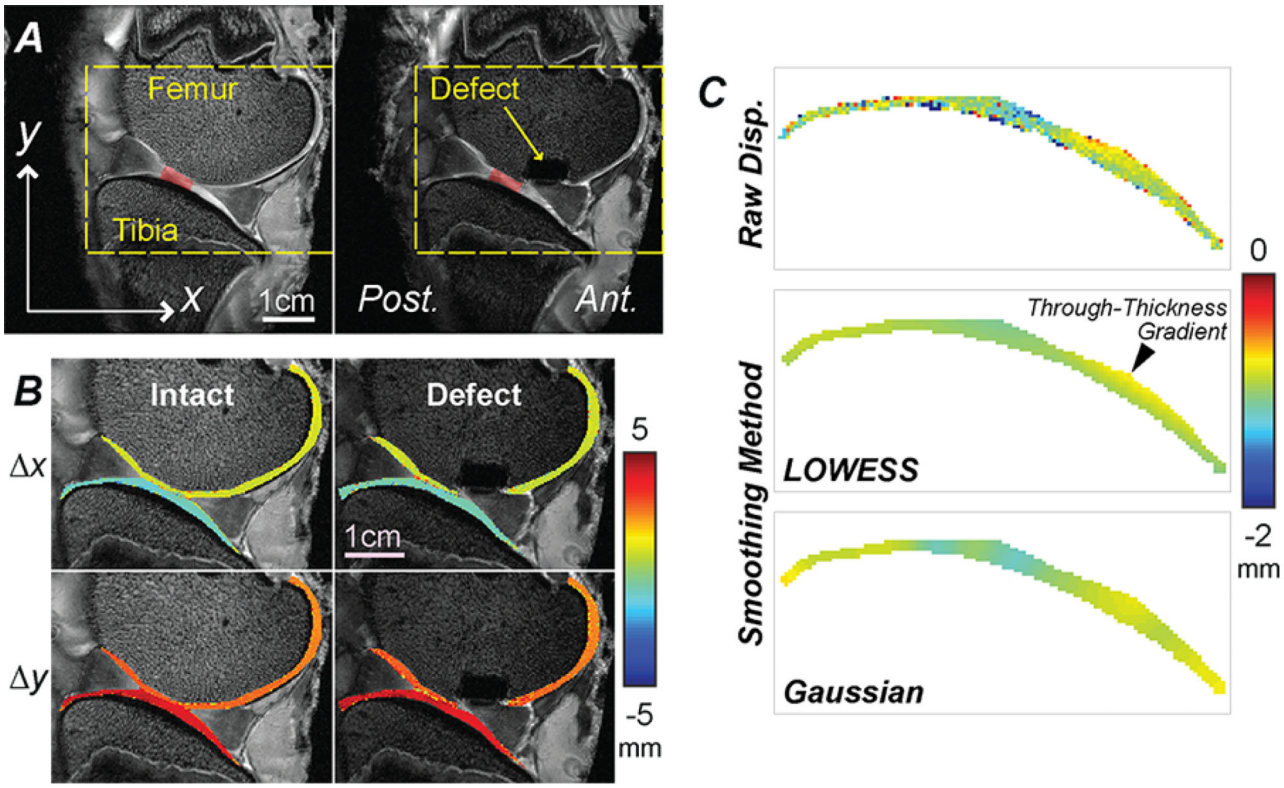

Figure 2. Spatial maps of displacements were noninvasively measured in articular cartilage before and following placement of a critical sized defect in the medial femoral condyle

Standard MRI of a representative specimen in intact and defect conditions allowed for the identification of a preserved cartilage-cartilage contact region (red shading), and registration of joint morphology in time-sequence MRI scans [*A*]. In-plane displacements were computed from dualMRI data [*B*] and show that rigid body motions dominate displacements in the loading direction (*y*) and direction transverse to loading (*x*), revealing little obvious internal spatial variations. [C] The raw displacements were smoothed using a locally-weighted linear regression (LOWESS) method, and showed expected through-thickness gradients, in contrast to Gaussian smoothing.

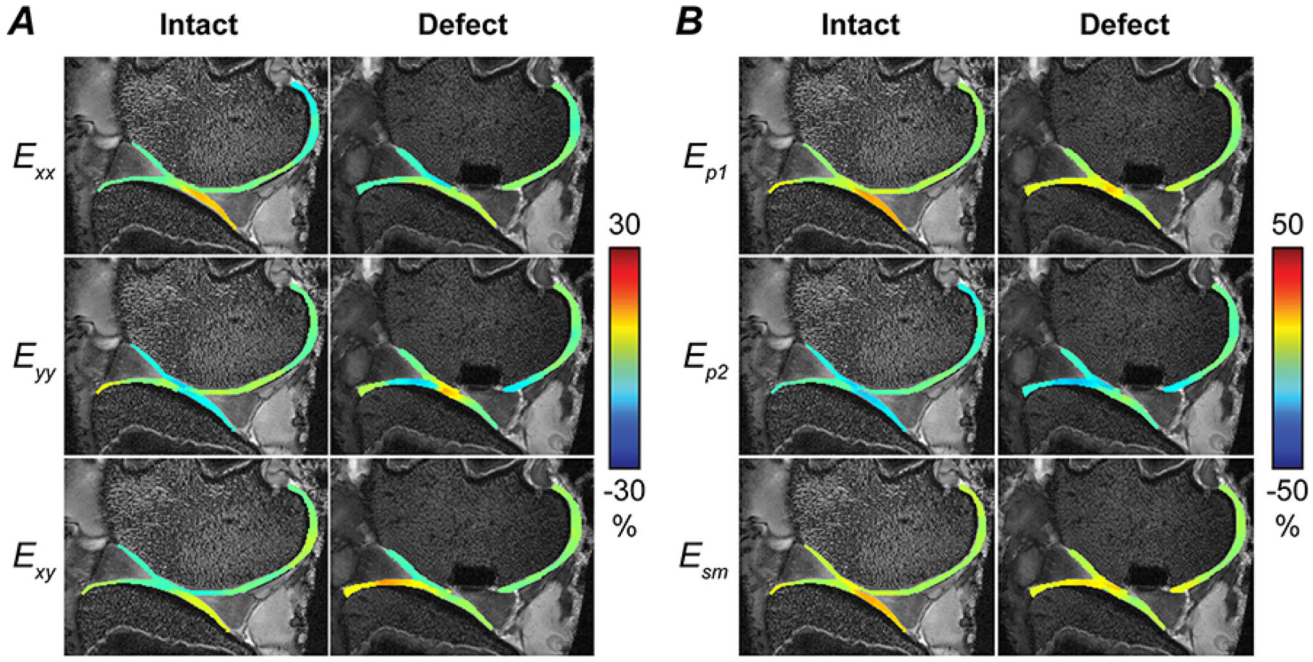

Figure 3. Spatial patterns of strain in articular cartilage increase and localize following creation of a full thickness defect

In-plane Green-Lagrange strains (E_{xx}, E_{yy}, E_{xy}) were computed from smoothed displacements [*A*], and first and second principal (E_{p1} and E_{p2}) and maximum shear (E_{sm}) strains were calculated [*B*]. High tensile and shear strains were observed at the interface between cartilage-cartilage and cartilage-meniscus contact areas in this representative specimen, with similar high-strain regions observed in other specimens.

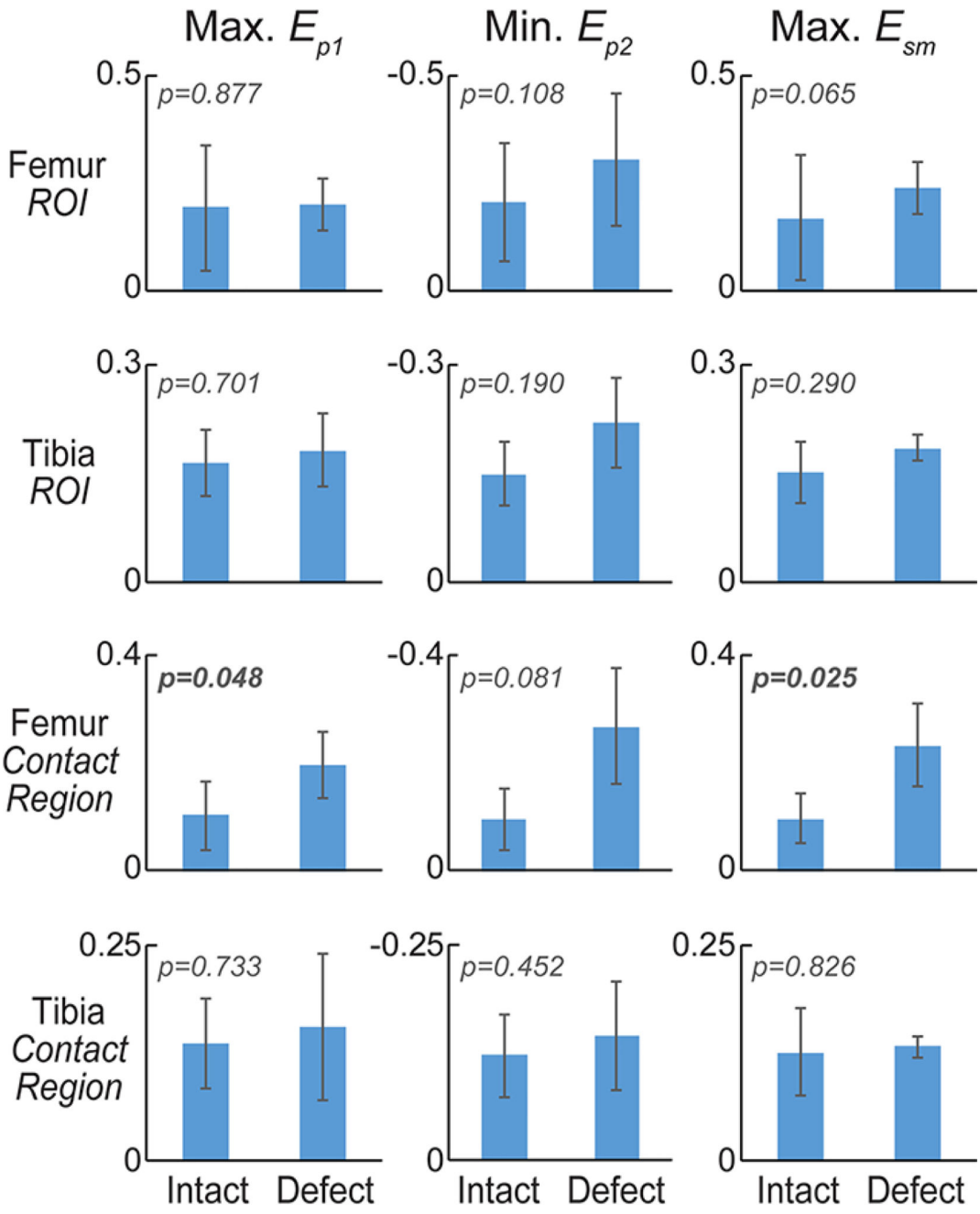

Figure 4. Maximum principal strains in cartilage tibia and femur regions of interest, and contact regions

Maximum values for first principal and maximum shear strain, and minimum values for second principal strain were computed for full tibial and femoral regions of interest (ROIs) in the intact and defect conditions [*A*]. The magnitude of principal strains tended to increase with defect placement in femoral, but not tibial, cartilage. Dramatic increases in the maximum shear strain within the contact region of femoral cartilage indicate a heightened sensitivity of this measure to defect placement and altered mechanics within the joint.

Table 1

Average principal strains in tibial cartilage contact regions

Minimal changes were observed in principal strains and maximum shear strain in the tibial cartilage following placement of a critical sized defect.

	Normal			Defect			Percentage Point *(i.e., Defect-Normal)*		
	E_{p1}	E_{p2}	E_{sm}	E_{p1}	E_{p2}	E_{sm}	E_{p1}	E_{p2}	E_{sm}
Sheep 1	8.0%	−6.7%	7.4%	12.0%	−2.9%	7.4%	4.0	3.8	0.1
Sheep 2	7.2%	−7.3%	7.3%	11.6%	−7.2%	9.4%	4.4	0.1	2.1
Sheep 3	3.8%	−2.4%	3.1%	8.3%	−6.5%	7.4%	4.6	−4.1	4.3
Sheep 4	12.1%	−9.5%	10.8%	−1.5%	−13.6%	6.1%	−13.6	−4.1	−4.7
Average	**7.8%**	**−6.5%**	**7.1%**	**7.6%**	**−7.6%**	**7.6%**	**−0.2**	**−1.1**	**0.5**

Percentage Point data were calculated from differences in raw data, and then rounded for presentation.

Table 2

Average principal strains in femoral cartilage contact regions

Principal strain changes were observed in the femoral condyle following placement of a critical sized defect.

	Normal			Defect			Percentage Point *(i.e., Defect-Normal)*		
	E_{p1}	E_{p2}	E_{sm}	E_{p1}	E_{p2}	E_{sm}	E_{p1}	E_{p2}	E_{sm}
Sheep 1	7.9%	−5.4%	6.6%	10.9%	−21.1%	16.0%	3.1	−15.7	9.4
Sheep 2	5.4%	−14.8%	10.1%	12.5%	−14.6%	13.5%	7.1	0.2	3.4
Sheep 3	10.4%	−4.5%	7.5%	11.6%	−28.9%	20.3%	1.3	−24.4	12.8
Sheep 4	1.0%	−2.4%	1.7%	16.4%	−16.1%	16.3%	15.4	−13.7	14.6
Average	**6.1%**	**−6.8%**	**6.5%**	**12.8%**	**−20.2%**	**16.5%**	**6.7**	**−13.4**	**10.0**

Percentage Point data were calculated from differences in raw data, and then rounded for presentation.